



Regulation of the central safety factor and normalized beta under low NBI torque in DIII-D

A. Pajares^{a,*}, E. Schuster^a, W.P. Wehner^b, K.H. Burrell^b, J.R. Ferron^b, M.L. Walker^b, D.A. Humphreys^b

^a Lehigh University, Bethlehem, PA 18015, USA

^b General Atomics, San Diego, CA 92121, USA

ARTICLE INFO

Keywords:

Safety factor control
Torque control
Low torque experiments

ABSTRACT

An algorithm has been designed to simultaneously control the central safety factor (q_0) and normalized beta (β_N) while ensuring near-zero torque from neutral beam injection in DIII-D. Feedback control of q_0 and β_N in tokamaks can be beneficial due to the close relationship that these variables have with plasma performance and magneto-hydrodynamic stability. In addition, low neutral-beam-torque conditions are of special interest in present devices because future burning-plasma tokamaks such as ITER will most likely operate at very low plasma rotation. The control synthesis of the algorithm presented in this work is based on a linearized, one-dimensional (1D) model of the current-profile dynamics coupled with a zero-dimensional (0D) plasma-energy balance. The actuators considered are neutral beam injection and electron-cyclotron heating and current drive, and discrete logic determines the neutral-beam injection powers that deliver near-zero torque. The algorithm has been tested in nonlinear, 1D simulations using COTSIM (Control-Oriented Transport Simulator) and in DIII-D experiments, demonstrating satisfactory performance.

1. Introduction

Most scaling laws predict an increase in the plasma-energy confinement time, τ_E , with the size of a tokamak [1,2]. This has motivated the design and construction of subsequently larger devices around the world, such as DIII-D (with a major radius $R_0 = 1.8$ m), TFTR (with $R_0 = 2.52$ m) or JET (with $R_0 = 2.96$ m) back in the 1980's, and more recently ITER ($R_0 = 6.2$ m), with the goal of attaining the necessary conditions for nuclear fusion. An increase in the machine size implies a higher plasma mass and moment of inertia, which translates into a lower plasma rotation produced by auxiliary sources. In contrast, present-day tokamaks often use neutral beam injectors (NBIs) which yield a plasma rotation much higher than the one expected in ITER [3]. Low rotation often causes "locking" of some magneto-hydrodynamic (MHD) modes, such as neoclassical tearing modes (NTMs), which may stop rotating and disrupt, potentially damaging the tokamak vessel and other plasma-facing components [4]. Although alternative sources of torque and rotation are currently being studied, like for example three-dimensional magnetic fields [5] and the intrinsic torque [6], ITER may need to operate at much lower rotation values than present devices.

Undesired MHD phenomena associated with low rotation may be avoided by achieving β_N and q_0 evolutions that diminish the chance of encountering MHD instabilities. It is a well-known fact predicted

by the theory [7] and observed in experiments [8] that β_N values near the ideal β_N -limit are usually related with a higher chance of NTM development. Control of β_N by means of feedback may aid to avoid and/or suppress NTMs [9], and also reduce the heat load to the machine components caused by disruptions [10]. On the other hand, high values of q_0 make low- q rational surfaces disappear from the plasma (here, q is the safety factor profile), particularly when q is monotonically increasing. Low- q surfaces are usually more prone to developing NTMs [11]. Therefore, having the capability of actively regulating q_0 and β_N by means of feedback can be highly beneficial for the realization of the ITER's mission. In addition, reproducing and studying ITER's conditions with low rotation (which is usually achieved at low NBI-torque in present devices) may provide valuable insights regarding MHD stability and performance for future reactor-sized tokamaks.

Significant research has been carried out to develop algorithms for q -profile regulation at several spatial locations, combined with β_N control (see, for example, [12–15]). Such work employs various control techniques such as nonlinear control, robust control, model-predictive control, and optimal control, among others. However, there are not many control solutions specialized for $q_0 + \beta_N$ regulation (see [16]) and, more importantly, no work can be found on simultaneous q_0, β_N ,

* Corresponding author.

E-mail address: pajaresa@fusion.gat.com (A. Pajares).

and NBI-torque control. In the present work, a control scheme for $q_0 + \beta_N + \text{NBI-torque}$ regulation is proposed that is based on a 1D model of the current-profile dynamics combined with a 0D energy balance. The plasma dynamics is linearized around a reference trajectory, and a control law is synthesized using pole-placement techniques [17] to regulate q_0 and β_N by means of the total NBI and electron-cyclotron heating and current drive (EC H&CD) powers, denoted by P_{NBI} and P_{EC} , respectively. The individual powers of the different NBIs are determined from P_{NBI} and P_{EC} utilizing discrete logic. Previous efforts along this line can be found in [18], in which solely q_0 regulation was considered. The control scheme for $q_0 + \beta_N + \text{NBI-torque}$ regulation has been tested using the nonlinear, 1D simulation code COTSIM [19], which employs 1D transport equations for the plasma energy, current, and momentum dynamics that are more complex than the model used for control synthesis. Moreover, experiments have been carried out in the DIII-D tokamak to assess the performance of the control scheme in quiescent H-mode (QH-mode) plasmas, i.e. H-mode plasmas which do not have edge localized modes [20], thus representing a scenario of high interest for ITER.

This paper is organized as follows. The plasma model for control synthesis is described in Section 2. The control synthesis is presented in Section 3. Section 4 includes simulation studies in DIII-D, QH-mode plasmas. Section 5 presents some initial experimental results obtained in DIII-D. Finally, a summary and conclusions are given in Section 6.

2. Control-synthesis modeling of the plasma current and energy dynamics

The poloidal stream function, ψ , is defined at a point P as

$$\psi \triangleq \int_{S_\theta} \vec{B}_\theta \cdot d\vec{S}_\theta, \quad (1)$$

where \vec{B}_θ is the poloidal magnetic field and \vec{S}_θ is the surface whose normal vector is \vec{z} and its boundary is the circumference centered at $R = 0$ which passes through P , as depicted in Fig. 1. Assuming toroidal symmetry and under ideal MHD conditions, a single coordinate can be employed to index the flux surfaces within the tokamak, as shown in Fig. 1. The mean effective minor radius, ρ , is the spatial coordinate used in this work. It is defined as

$$\rho \triangleq \sqrt{\frac{\Phi}{B_{\phi,0}\pi}}, \quad (2)$$

where $\Phi = \int_{S_\phi} \vec{B}_\phi \cdot d\vec{S}_\phi$ is the toroidal flux (see Fig. 1, where \vec{S}_ϕ is the surface whose normal vector is $\vec{\phi}$ and its boundary is defined by the magnetic-flux surface contour in the $r - z$ plane, and \vec{B}_ϕ is the toroidal magnetic field), and $B_{\phi,0}$ is the vacuum, toroidal magnetic-field of reference at the geometric axis. The normalized mean effective minor radius is given by $\hat{\rho} \triangleq \rho/\rho_b$, where ρ_b is the value of ρ at the last closed magnetic-flux surface.

The central safety factor, q_0 , is the value of q at $\hat{\rho} = 0$, and it is defined as

$$q_0 \triangleq - \left. \frac{B_{\phi,0}\hat{\rho}\rho_b^2}{\partial\psi/\partial\hat{\rho}} \right|_{\hat{\rho}=0} = - \left. \frac{B_{\phi,0}\rho_b^2}{\partial^2\psi/\partial\hat{\rho}^2} \right|_{\hat{\rho}=0}, \quad (3)$$

where L'Hopital's rule has been employed (it must be noted that $\partial\psi/\partial\hat{\rho}|_{\hat{\rho}=0} = 0$ due to symmetry about the magnetic axis, see Fig. 1). The normalized beta, β_N , and toroidal beta, β_t , are defined as

$$\beta_N \triangleq \frac{aB_{\phi,0}}{I_p} \beta_t [\%], \quad (4)$$

$$\beta_t \triangleq \frac{1}{V_p} \frac{\frac{2}{3}W}{B_{\phi,0}^2/(2\mu_0)}, \quad (5)$$

where a is the minor radius, I_p is the total plasma current, W is the thermal stored energy, V_p is the plasma volume, and μ_0 is the vacuum permeability.

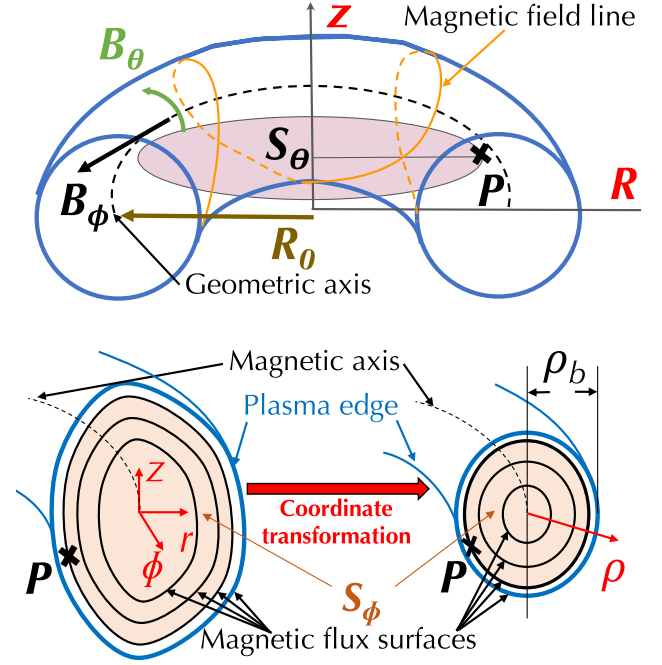


Fig. 1. Diagram of the magnetic fields and flux surfaces in a tokamak. At the top, the magnetic field components, B_ϕ and B_θ , and surface S_θ are shown together with a 3D representation of a tokamak plasma. At the bottom, flux-surface geometry in $r - z - \phi$ coordinates (on the left) and equivalent ρ coordinate representation (on the right) after the coordinate transformation, together with the surface S_ϕ .

The model employed for the dynamics of $\psi(\hat{\rho}, t)$ is based on the magnetic-diffusion equation (see Appendix A for details),

$$\begin{aligned} \frac{\partial\psi(\hat{\rho}, t)}{\partial t} &= f_{\eta,1}(\hat{\rho}) \frac{\partial}{\partial\hat{\rho}} \left(f_{\eta,2}(\hat{\rho}) \frac{\partial\psi(\hat{\rho}, t)}{\partial\hat{\rho}} \right) u_\eta(t) + \\ &+ \sum_{j=1}^{j=N_{NBI}} f_{NBI,j}(\hat{\rho}, t) \frac{P_{NBI,j}(t)}{P_{tot}(t)} + f_{EC}(\hat{\rho}, t) \frac{P_{EC}(t)}{\sqrt{P_{tot}(t)}} + \\ &+ f_{BS}(\hat{\rho}) \left(\frac{\partial\psi(\hat{\rho}, t)}{\partial\hat{\rho}} \right)^{-1} u_{BS}(t), \end{aligned} \quad (6)$$

together with its boundary conditions,

$$\left. \frac{\partial\psi}{\partial\hat{\rho}} \right|_{(\hat{\rho}=0,t)} = 0, \quad (7)$$

$$\left. \frac{\partial\psi}{\partial\hat{\rho}} \right|_{(\hat{\rho}=1,t)} = -k_{I_p} I_p(t), \quad (8)$$

where $f_{\eta,1}$ and $f_{\eta,2}$ are spatial profiles related with the flux-diffusion mechanism, $f_{NBI,j}$ (for $j = 1, \dots, N_{NBI}$, where N_{NBI} is the total number of NBIs) are spatial profiles that characterize the current deposition of the NBIs, f_{EC} is a spatial profile that characterizes the ECCD, f_{BS} is a spatial profile that model the bootstrap-current deposition (all the model profiles f_{\cdot} depend on the plasma equilibrium, as detailed in Appendix A), $P_{NBI,j}$ is the power of the j th NBI (i.e. $\sum_{j=1}^{j=N_{NBI}} P_{NBI,j} \triangleq P_{NBI}$), P_{EC} is the total ECH & CD power, $P_{tot} \triangleq P_{NBI} + P_{EC}$ is the total injected power, k_{I_p} is a model parameter that depends on the plasma equilibrium, and u_η and u_{BS} are virtual inputs given by

$$u_\eta = \left(I_p \sqrt{P_{tot}} \right)^{-3/2}, \quad (9)$$

$$u_{BS} = \left(I_p \sqrt{P_{tot}} \right)^{-1/2} \bar{n}_e, \quad (10)$$

where \bar{n}_e is the line-average electron density. Both I_p and \bar{n}_e are not directly regulated by the control algorithm, so they are treated as non-controllable inputs to the system. These virtual inputs u_η and u_{BS} arise from the models employed for the plasma resistivity, bootstrap current,

auxiliary-source current, electron density, and electron temperature (see Appendix A for details).

The dynamics of the thermal stored energy $W(t)$ is modeled by

$$\frac{dW}{dt} = -\frac{W}{\tau_E} + P_{tot}, \quad (11)$$

where τ_E is the energy confinement time, which is modeled by the IPB98(y,2) scaling,

$$\tau_E = 0.0562 H_{98(y,2)} I_p^{0.93} B_{\phi,0}^{0.15} A_{eff}^{0.19} R_0^{1.98} \epsilon^{0.58} \kappa^{0.78} P_{tot}^{-0.69} \bar{n}_e^{-0.41},$$

where $H_{98(y,2)}$ is a constant parameter that characterizes the plasma-confinement quality ($H_{98(y,2)} = 1$ represents the best fit to experimental data [21]), A_{eff} is the effective plasma mass, $\epsilon \triangleq a/R_0$ is the inverse aspect ratio (where R_0 is the major radius) and κ is the plasma elongation.

In this work, it is assumed that the net current driven by the NBIs is very low when compared to other sources of current. Because the NBIs are employed in a balanced configuration to produce near-zero torque, the current injected by co-current NBIs will be mostly cancelled out by the current injected by the counter-current NBIs. This implies that the second term on the right-hand side of (6) is very small when compared to the other sources of current. Therefore, the main contribution of the individual NBI powers, $P_{NBI,i}$, is to the total NBI power, P_{NBI} , as a heating source (i.e. within P_{tot}). As a result, P_{NBI} is considered as a single controllable input within the pole-placement design presented in this work (see Section 3.3), and $P_{NBI,i}$ are subsequently determined from P_{NBI} in order to deliver near-zero torque by using discrete logic (see Section 3.4). In addition, from Eq. (6), it can be seen that P_{EC} is considered as a single controllable input that groups several ECH & CD sources as a unique cluster. More details can be found in Appendix A.

To summarize, the state of the nonlinear, distributed-parameter model described in this section is given by $\hat{x} \triangleq [\psi, W]^T$, the output vector is $y \triangleq [q_0, \beta_N]^T$, the controllable input is $u \triangleq [P_{NBI}, P_{EC}]^T$, the non-controllable input is $v \triangleq [I_p, \bar{n}_e]^T$, the state equation consists of (6) and (11) (together with (7)–(8)), and the output equation is given by (3)–(5).

3. Control synthesis using pole-placement techniques and discrete logic

3.1. Space discretization of the current-profile dynamics

In order to transform the distributed-parameter (infinite dimensional) model from Section 2 into a lumped-parameter (finite dimensional) model that is more tractable for control synthesis, the magnetic-diffusion equation (6) and its boundary conditions (7)–(8) are discretized in space using the finite-differences method. A total number of $N + 2$ nodes are employed in the spatial domain $\hat{\rho} = [0, 1]$, so there are two boundary nodes ($\hat{\rho}_0 = 0$ and $\hat{\rho}_{N+1} = 1$) and N interior nodes ($\hat{\rho}_i = i\Delta\hat{\rho}$, for $i = 1, 2, \dots, N$, where $\Delta\hat{\rho} = 1/(N + 1)$ is the discretization step). Therefore, the state equation composed of (6) and (11) can be rewritten as

$$\frac{d\hat{x}}{dt} = f(x, u, v), \quad (12)$$

where $x \triangleq [\psi_1, \dots, \psi_N, W]^T \in \mathbb{R}^{N+1}$ is the state vector of the lumped-parameter model, $\psi_i(t) \triangleq \psi(\hat{\rho}_i, t)$, and $f \in \mathbb{R}^{N+1}$ is a nonlinear state-function arising from the discretization of (6)–(8) plus (11). It must be noted that the values of ψ at $\hat{\rho}_0 = 0$ and $\hat{\rho}_{N+1} = 1$ are not included within the system's state vector x because the boundary conditions (7)–(8) allow for expressing them in terms of ψ at the interior nodes. In a similar way, the output equation given by (3)–(5) can be rewritten as

$$y = g(x, u, v), \quad (13)$$

where $g \in \mathbb{R}^2$ is a nonlinear output-function. Eqs. (12)–(13) model a lumped-parameter, nonlinear system. More details can be found in Appendix B.

3.2. Linearization of the current-profile and energy dynamics

Next, the spatially-discretized, nonlinear model given by (12)–(13) is linearized around a nominal evolution. The nominal evolutions for the outputs q_0 and β_N are denoted by \bar{q}_0 and $\bar{\beta}_N$, respectively. For convenience, deviation variables are defined for the outputs as $\bar{q}_0 \triangleq q_0 - \bar{q}_0$, $\bar{\beta}_N \triangleq \beta_N - \bar{\beta}_N$, and $\bar{y} \triangleq y - \bar{y}$, where $\bar{y} = [\bar{q}_0, \bar{\beta}_N]^T$. Also, the deviation variable for the state vector is given by $\bar{x} \triangleq x - \bar{x}$, where $\bar{x} \triangleq [\bar{\psi}_1, \dots, \bar{\psi}_N, \bar{W}]^T$ contains the equilibrium evolution for ψ at the interior nodes ($\hat{\rho}_1, \hat{\rho}_2, \dots, \hat{\rho}_N$) together with the equilibrium evolution for W . The controllable and non-controllable inputs associated with the equilibrium evolution are denoted by \bar{u} and \bar{v} , respectively, and the deviation vectors for them are denoted by $\bar{u} \triangleq u - \bar{u}$ and $\bar{v} \triangleq v - \bar{v}$, respectively.

Therefore, the nominal dynamics is obtained from (12)–(13) as given by

$$\frac{d\bar{x}}{dt} = f(\bar{x}, \bar{u}, \bar{v}), \quad \bar{y} = g(\bar{x}, \bar{u}, \bar{v}), \quad (14)$$

and the dynamics of the deviation variables is given by

$$\frac{d\bar{x}}{dt} = f(\bar{x} + \bar{x}, \bar{u} + \bar{u}, \bar{v} + \bar{v}) - f(\bar{x}, \bar{u}, \bar{v}) \triangleq \tilde{f}(\bar{x}, \bar{u}, \bar{v}, t), \quad (15)$$

$$\bar{y} = g(\bar{x} + \bar{x}, \bar{u} + \bar{u}, \bar{v} + \bar{v}) - g(\bar{x}, \bar{u}, \bar{v}) \triangleq \tilde{g}(\bar{x}, \bar{u}, \bar{v}, t). \quad (16)$$

The deviation dynamics (15)–(16) can be linearized around the nominal evolution defined by \bar{x} , \bar{u} , and \bar{v} as given by

$$\frac{d\bar{x}}{dt} = A\bar{x} + B\bar{u} + B'\bar{v}, \quad (17)$$

$$\bar{y} = C\bar{x} + D\bar{u} + D'\bar{v}, \quad (18)$$

where

$$A \triangleq \left. \frac{\partial \tilde{f}}{\partial \bar{x}} \right|_{\bar{x}, \bar{u}, \bar{v}} \in \mathbb{R}^{(N+1) \times (N+1)}, \quad (19)$$

$$B \triangleq \left. \frac{\partial \tilde{f}}{\partial \bar{u}} \right|_{\bar{x}, \bar{u}, \bar{v}} \in \mathbb{R}^{(N+1) \times 2}, \quad B' \triangleq \left. \frac{\partial \tilde{f}}{\partial \bar{v}} \right|_{\bar{x}, \bar{u}, \bar{v}} \in \mathbb{R}^{(N+1) \times 2}, \quad (20)$$

$$C \triangleq \left. \frac{\partial \tilde{g}}{\partial \bar{x}} \right|_{\bar{x}, \bar{u}, \bar{v}} \in \mathbb{R}^{2 \times (N+1)}, \quad (21)$$

$$D \triangleq \left. \frac{\partial \tilde{g}}{\partial \bar{u}} \right|_{\bar{x}, \bar{u}, \bar{v}} \in \mathbb{R}^{2 \times 2}, \quad D' \triangleq \left. \frac{\partial \tilde{g}}{\partial \bar{v}} \right|_{\bar{x}, \bar{u}, \bar{v}} \in \mathbb{R}^{2 \times 2}. \quad (22)$$

By means of linearization around a nominal evolution, the nonlinear model in (12)–(13) has been approximated by the linear, time-varying model (17)–(18) with model matrices given by (19)–(22).

3.3. Control laws for P_{NBI} and P_{EC} using pole placement

The first goal of the control scheme is to regulate \bar{q}_0 and $\bar{\beta}_N$ around some targets denoted as q_0^{target} and β_N^{target} , respectively, while also rejecting the perturbations arising from the non-controllable input \bar{v} . The target output is denoted by $y^{target} = [q_0^{target}, \beta_N^{target}]^T$. An output-feedback control law is employed,

$$\bar{u} = -K_p (\bar{y} - y^{target}) - K_I \int_{t_0}^t (\bar{y} - y^{target}) dt, \quad (23)$$

where t_0 is the initial time when the feedback-control law is started, and $K_p \in \mathbb{R}^{2 \times 2}$ and $K_I \in \mathbb{R}^{2 \times 2}$ are design matrices that are determined as explained next. By applying the Laplace transform to (17)–(18), using (23), and solving for \bar{y} , it is possible to write

$$\bar{Y} = [(I + GK)^{-1} GK] Y^{target} + [(I + GK)^{-1} G'] \bar{V}, \quad (24)$$

where \bar{Y} , Y^{target} , and \bar{V} are the Laplace transforms of \bar{y} , y^{target} , and \bar{v} , respectively, and $K \triangleq K_p + K_I s^{-1}$, where s is the Laplace variable [17]. The matrices given by

$$G \triangleq [C(sI - A)^{-1} B + D], \quad (25)$$

$$G' \triangleq [C(sI - A)^{-1} B' + D'] \quad (26)$$

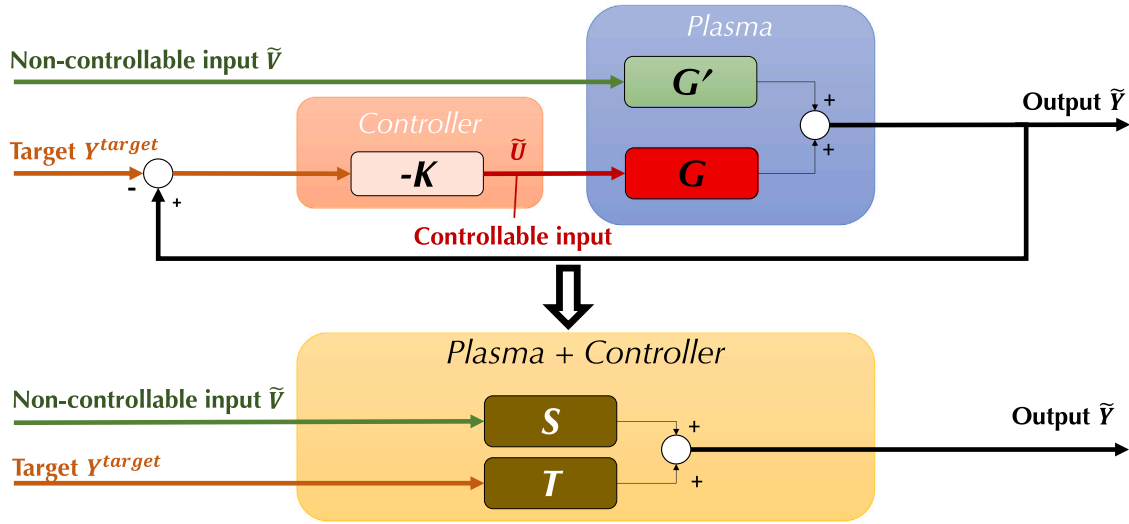


Fig. 2. Block diagram showing the plasma open-loop transfer functions G (from the controllable input \tilde{U} to the output \tilde{Y} , shown in red) and G' (from the non-controllable input \tilde{V} to the output \tilde{Y} , shown in green), the controller K (shown in orange), the target Y^{target} , and the equivalent compact representation of the plasma and controller (shown in yellow) using the transfer functions $T \triangleq (I + GK)^{-1} GK$ and $S \triangleq (I + GK)^{-1} G'$ (shown in brown).

are the input–output and disturbance–output transfer functions, respectively. Both G and G' are 2×2 matrices. Therefore, from (24), the closed-loop transfer functions given by

$$T \triangleq (I + GK)^{-1} GK, \quad (27)$$

$$S \triangleq (I + GK)^{-1} G', \quad (28)$$

characterize how \tilde{Y} tracks Y^{target} (in the case of T) and is disturbed by \tilde{V} (in the case of S). Both S and T are also 2×2 matrices. Fig. 2 shows a block diagram illustrating the connections between targets, inputs, outputs, and transfer functions. The design of T and S (which is done through K) is carried out in this work using pole-placement techniques [17] to ensure the desired closed-loop performance of the system.

Some characteristics of the open-loop dynamics (17)–(18) are described next in order to motivate the subsequent design choices for T and S . First, stabilizing (17)–(18) is not a goal because all its poles are on the left-half of the s plane. Such open-loop stability can also be inferred from the diffusive current and heat transport mechanisms present in the magnetic-diffusion equation (6) and energy balance (11). The characteristic times for these diffusive processes are introduced next. The current-diffusion time [7] is given by $\tau_R \triangleq \mu_0 a^2 / \eta$ (where η is the plasma resistivity), and is of the order of $\tau_R \approx [1, 10]$ s in DIII-D. The energy-confinement time is between $\tau_E \approx 10$ ms and $\tau_E \approx 100$ ms for QH-mode plasmas in DIII-D [20]. These characteristic times are related to the open-loop poles, which for the plasmas in this work are as follows. First, one pure-real pole exists which corresponds to the fast W dynamics. This pole is located around $s \approx -20$ (i.e. $\tau_E \approx 50$ ms). Second, about $N/3$ pairs of complex conjugate poles are found for the fast oscillatory modes of the ψ dynamics. These poles are located at around $s \approx -5 \pm 0.5j$. Finally, about $N/3$ poles correspond to slow, non-oscillatory modes of the ψ dynamics located on the real axis between $s \approx -1$ and $s \approx -0.1$ (i.e. $\tau_R \approx 1 - 10$ s).

The objective of the pole-placement design is to relocate the slow poles at $s \approx [-1, -0.1]$ toward $s \approx -10$. This makes the ψ dynamical timescale comparable to the W dynamical timescale, so both tracking (through T) and disturbance rejection (through S) become faster with timescales relevant for a discharge duration, which is usually about 6 s in DIII-D. In general, relocation of these slow poles cannot be formally ensured by the use of an output-feedback law such as (23). However, in practice, if $N = 9$ (i.e. $\hat{\rho} = [0, 0.1, \dots, 0.9, 1]$, see Section 3.1) the 8 tunable gains in K_p and K_I are sufficient to relocate the 3 slow poles to $s \approx -10$. It must be noted that K_p and K_I are fully populated matrices

due to the high degree of coupling found between the outputs, q_0 and β_N , and inputs, P_{NBI} and P_{EC} (see Appendix C).

Once K is designed, the control law (23) provides the value of \tilde{u} in real time, so the closed-loop value for the controllable input, $u = \tilde{u} + \tilde{u}$, can be calculated. The two components of u are denoted by P_{NBI}^{req} and P_{EC}^{req} , i.e. $u = [P_{NBI}^{req}, P_{EC}^{req}]^T$ (the superscript “req” stands for “request”). It must be noted that (17)–(18) is a linear approximation of the nonlinear plasma dynamics around \bar{x} , \bar{u} , and \bar{v} that is valid as long as the norms of \tilde{y} (and y^{target}), \tilde{u} , and \tilde{v} are small. The controller in (23) will indeed keep such norms small as long as the initial deviations \tilde{y} and \tilde{v} are also small enough and can be controlled [17].

3.4. Discrete logic for $P_{NBI,i}$ to deliver near-zero NBI torque

The second goal of the control scheme is to ensure that the NBIs are balanced to deliver as low torque as possible. This is done by calculating $P_{NBI,i}$ from P_{NBI}^{req} using discrete logic. In this work, the DIII-D tokamak is considered with 6 co-current NBIs (whose powers are denoted by $P_{30}^R, P_{150}^R, P_{150}^L, P_{150}^R, P_{330}^L, P_{330}^R$) and 2 counter-current NBIs (whose powers are denoted by P_{210}^L and P_{210}^R), so $N_{NBI} = 8$. The NBIs are divided in two groups which are also balanced, i.e., a 1st group with 30L, 150L, 210R, and 330L, and a 2nd group with 30R, 150R, 210L, and 330R. Each group has three co-current NBIs and one counter-current NBI, so that their powers fulfill the following relationships,

$$P_{30}^L + P_{30}^R + P_{150}^L + P_{150}^R + P_{210}^L + P_{210}^R + P_{330}^L + P_{330}^R = P_{NBI}^{req}, \quad (29)$$

$$\text{1st group: } P_{30}^L + P_{150}^L + P_{330}^L = P_{210}^R, \quad (30)$$

$$\text{2nd group: } P_{30}^R + P_{150}^R + P_{330}^R = P_{210}^L. \quad (31)$$

Because there are more unknowns ($N_{NBI} = 8$, i.e. 8 individual NBI powers) than equations, the linear system given by (29)–(31) does not uniquely determine $P_{NBI,i}$.

The following practical considerations add constraints to the problem and allow for obtaining a unique solution. First, in order to obtain motional stark effect (MSE) measurements for more accurate internal equilibrium reconstructions in DIII-D, P_{30}^L is modulated to deliver a fixed power denoted by $P_{30}^{L,MSE}$. In addition, 30R must be turned off or modulated off-phase with 30L (otherwise, 30R would interfere with 30L and MSE measurements would not be available). Therefore, the power delivered by 30R is also fixed and denoted as $P_{30}^{R,MSE}$.

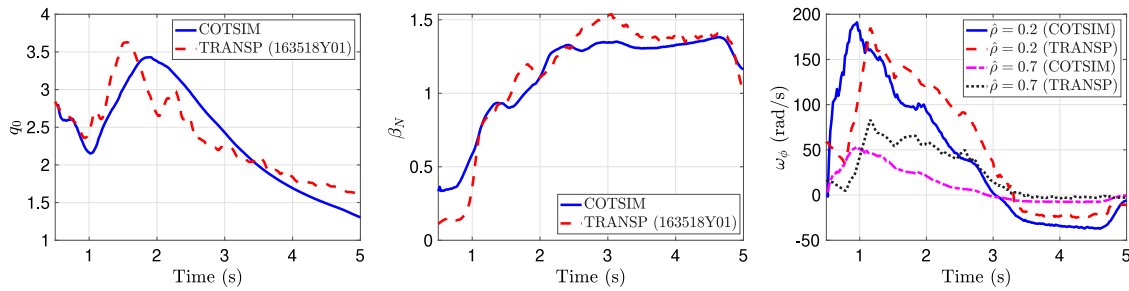


Fig. 3. Time evolutions for q_0 , β_N , and ω_ϕ in feedforward-only simulations using COTSIM (solid blue) and TRANSP (dashed red).

Second, in order to even out the amount of power that every NBI needs to deliver, it is imposed that the two balanced-NBI groups deliver the same power.

Third, the 150 beamline (i.e. where the 150L and 150R NBIs are installed) has a smaller size and different ion source than the 30, 210, and 330 beamlines. In order to produce the same power, the 150 beamline requires higher voltage than the other beamlines. Running at higher voltages is sometimes associated with a lower beamline reliability. In order to prioritize the robustness against actuator failures of the overall control scheme, the 150 beamline is kept as a backup beamline to achieve beam balancing only when the 330 beamline is failing. Despite the smaller size of the 150 beamline, it can produce enough power to substitute the 330 beamline in a balanced configuration (see Sections 4 and 5). However, it must be kept in mind that, because the 30 beamline is essential for MSE, it cannot be substituted by the 150 beamline.

As a summary, $P_{NBI,i}$ are determined from P_{NBI}^{req} using the following equations and logic:

1. Feedback control law:

$$P_{30}^L + P_{30}^R + P_{150}^L + P_{150}^R + P_{330}^L + P_{330}^R + P_{210}^L + P_{210}^R = P_{NBI}^{req}. \quad (32)$$

2. Beam balancing:

$$P_{30}^{L,MSE} + P_{150}^L + P_{330}^L = P_{210}^R, \quad (33)$$

$$P_{30}^{R,MSE} + P_{150}^R + P_{330}^R = P_{210}^L. \quad (34)$$

3. Practical consideration 1: 30 beamline used for MSE

$$P_{30}^L = P_{30}^{L,MSE}, \quad (35)$$

$$P_{30}^R = P_{30}^{R,MSE}. \quad (36)$$

4. Practical consideration 2: equal balanced-group power

$$P_{30}^{L,MSE} + P_{150}^L + P_{330}^L + P_{210}^R = P_{30}^{R,MSE} + P_{150}^R + P_{330}^R + P_{210}^L. \quad (37)$$

5. Practical consideration 3: check 330 beamline availability

$$\text{If 330L is available, set } P_{150}^L = 0, \text{ or} \quad (38a)$$

$$\text{If 330L is unavailable, set } P_{330}^L = 0. \quad (38b)$$

$$\text{If 330R is available, set } P_{150}^R = 0, \text{ or} \quad (39a)$$

$$\text{If 330R is unavailable, set } P_{330}^R = 0. \quad (39b)$$

6. Solve the linear system (32)–(39) for the unknowns P_{30}^L , P_{30}^R , P_{150}^L , P_{150}^R , P_{210}^L , P_{210}^R , P_{330}^L , and P_{330}^R .

It can be seen that (32)–(39) is a system of 8 equations with 8 unknowns that always has a solution and uniquely determines $P_{NBI,i}$. It must also be noted that actuator-saturation constraints (i.e. limits on the attainable $P_{NBI,i}$) are not included because, if they are temporarily incompatible with (32)–(39), the overall problem becomes infeasible. In other words, this is not a limitation of the controller itself, but it arises from the impossibility of achieving near-zero NBI torque, MSE measurements, unsaturated inputs, and successful $q_0 + \beta_N$ control all simultaneously during some periods of time.

4. Nonlinear, 1D simulation testing in COTSIM

4.1. Comparison between COTSIM and TRANSP simulations

In this section, COTSIM results are shown for a feedforward-only simulation (i.e. no feedback control) that uses the experimental inputs of DIII-D, QH-mode shot 163518. This feedforward COTSIM simulation is compared with a predictive TRANSP [22] simulation (163518Y02) which also uses the same experimental inputs. It must be clarified that shot 163518 was attained in experiments prior to this work, so it did not employ the $q_0 + \beta_N + \text{NBI-torque}$ feedback algorithm.

The models implemented in COTSIM for this work are as follows. First, the magnetic-diffusion equation is implemented with the Spitzer model for the plasma resistivity, the Sauter model for the bootstrap current, and control-oriented models of the auxiliary-current deposition [23]. Second, an electron heat-transport equation is used with a thermal-diffusivity model that includes a mixed Bohm/Gyro-Bohm model [24] for anomalous transport as well as neoclassical transport contributions [25]. Also, control-oriented models of the electron-power deposition are used, together with a theory-based pedestal model [26]. Third, an ion toroidal-momentum equation is used with a simplified momentum-diffusivity model and control-oriented models of the torque deposition [27]. On the other hand, TRANSP employs a magnetic-diffusion equation, heat-transport equation, and ion toroidal-momentum equation that are very similar to those implemented in COTSIM, as well as Spitzer, Sauter, and neoclassical transport models. However, the current, power, and torque sources as well as the anomalous-transport contribution and pedestal dynamics are characterized by models which are significantly more complex [22], such as the TGLF transport model [28] or the NUBEAM model for NBI heating, current drive, and torque [29]. It must be taken into account that COTSIM can simulate a shot significantly faster than TRANSP (i.e. a few second in COTSIM, but a few hours in TRANSP) at the expense of using relatively simpler models. Still, COTSIM does simulate much of the relevant plasma dynamics that is necessary for control design, and allows for fast tuning and simulation testing of feedback controllers. More details on the models that COTSIM may employ can be found, for example, in [19].

Fig. 3 shows the time evolution of the outputs, q_0 and β_N , as well as the toroidal rotation, ω_ϕ , at two locations. Fig. 4 shows the experimental inputs $P_{NBI,i}$ from shot 163518 ($P_{30}^R \equiv 0$, $P_{330}^L \equiv 0$, and $P_{EC} \equiv 0$ in this shot). From Fig. 3, it can be seen that COTSIM calculates evolutions for β_N , q_0 , and ω_ϕ that follow very similar trends to those calculated by TRANSP. Therefore, COTSIM is capable of simulating these DIII-D, QH-mode plasmas reasonably well. Finally, from Fig. 4, it can be observed that the plasma initially has some significant co-current torque, and the counter-current NBIs are progressively turned on to achieve full balance only after $t \approx 2.5$ s. It can also be observed that the power modulation in the 30 beamline does not ensure MSE measurements during the whole shot.

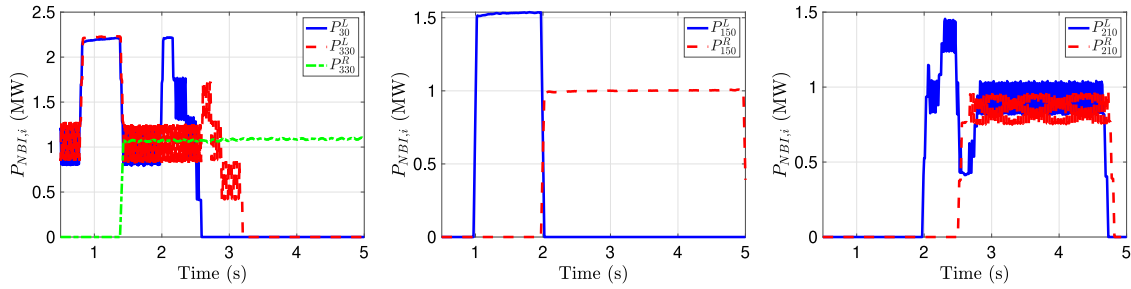


Fig. 4. Time evolutions for $P_{NBI,i}$ employed in feedforward-only simulations, corresponding to the experimental inputs during DIII-D shot 163518.

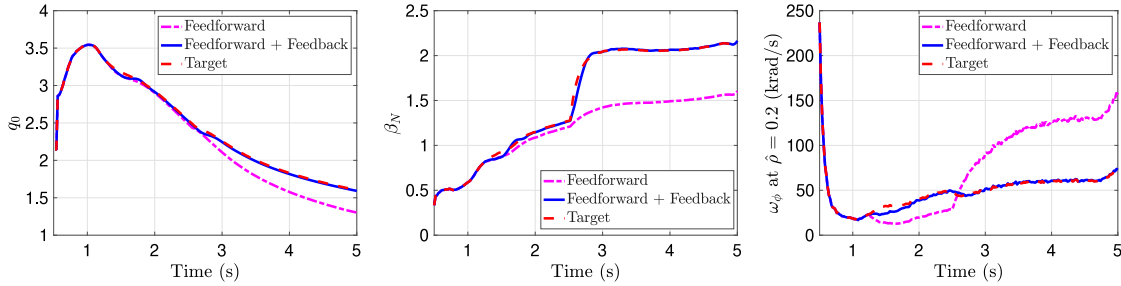


Fig. 5. Time evolutions simulated with COTSIM for q_0 , β_N , and ω_ϕ at $\rho = 0.2$ in feedforward (dashed-dotted magenta) and feedforward + feedback (solid blue), together with the targets (dashed red).

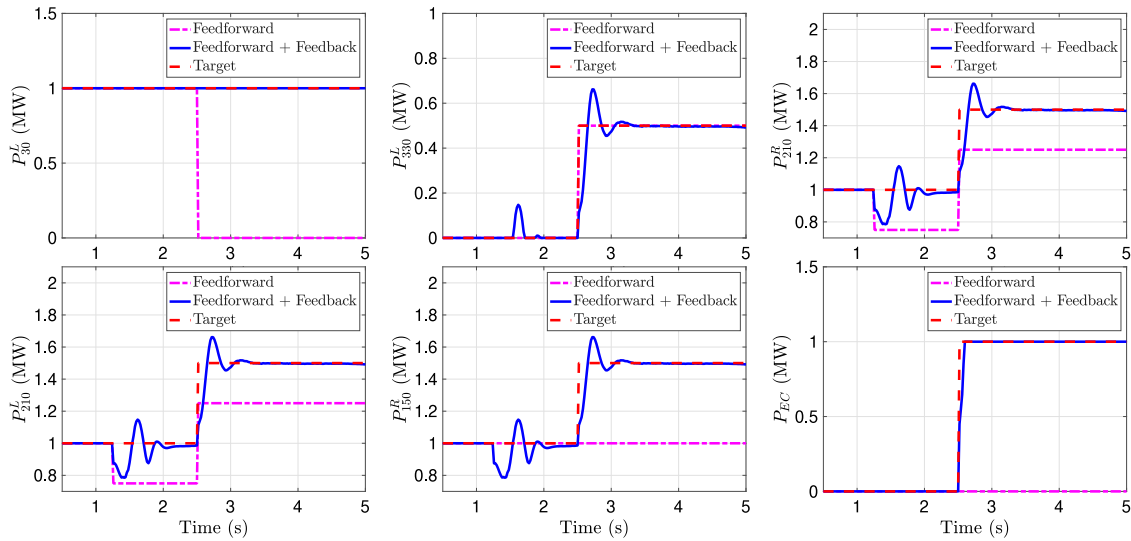


Fig. 6. Time evolutions in COTSIM for $P_{NBI,i}$ and P_{EC} in feedforward (dashed-dotted magenta), target (dashed red), and feedforward + feedback (solid blue).

4.2. Feedforward + feedback testing

In this section, COTSIM results are shown to demonstrate the tracking performance of the feedforward + feedback scheme. The models employed in COTSIM are the same as those described in Section 4.1. The goal is testing whether q_0 and β_N can track the associated targets (denoted as q_0^{target} and β_N^{target}) by using the feedback controller, similarly to what would be expected from the algorithm in an experiment. The following simulations are carried out. First, a feedforward-only simulation is executed where the balanced-NBI configuration is not used and (35)–(36) are not enforced (i.e. if this feedforward was used in an experiment, there would be no guarantee of MSE measurements). The inputs for this simulation correspond to the dashed-dotted magenta evolutions in Fig. 6. These inputs are denoted as $\bar{u}^{FF,1}$. A second feedforward simulation is run with inputs that use the balanced configuration described in Section 3.4, where $P_{30}^{L,MSE} = 1$ MW and

$P_{30}^{R,MSE} = 0$ (the inputs for this simulation correspond to the dashed-red evolutions in Fig. 6). Such inputs are denoted by $\bar{u}^{FF,2}$, and the q_0 and β_N evolutions obtained in this second simulation are set as q_0^{target} and β_N^{target} , respectively. Finally, a third simulation in feedforward + feedback is executed using the feedforward inputs from the first simulation, i.e. $\bar{u} = \bar{u}^{FF,1}$, plus the feedback component \tilde{u} calculated by the controller. The inputs for this feedforward + feedback simulation (i.e. $u = \bar{u}^{FF,1} + \tilde{u}$) are the solid blue evolutions in Fig. 6, where the near-zero NBI-torque feedback starts at $t = 1.25$ s. It must be emphasized that the controller does not have any knowledge of the feedforward inputs $\bar{u}^{FF,2}$ used to generate the targets, and that it uses $\bar{u} = \bar{u}^{FF,1}$ as its feedforward instead. Because $\bar{u}^{FF,1} \neq \bar{u}^{FF,2}$, achieving zero tracking-error necessarily requires $\tilde{u} \neq 0$. Also, different NBI combinations are tested by emulating that 330R fails and is replaced by 150R, and also that 330L can be used, so 150L is not needed (see (38)–(39)).

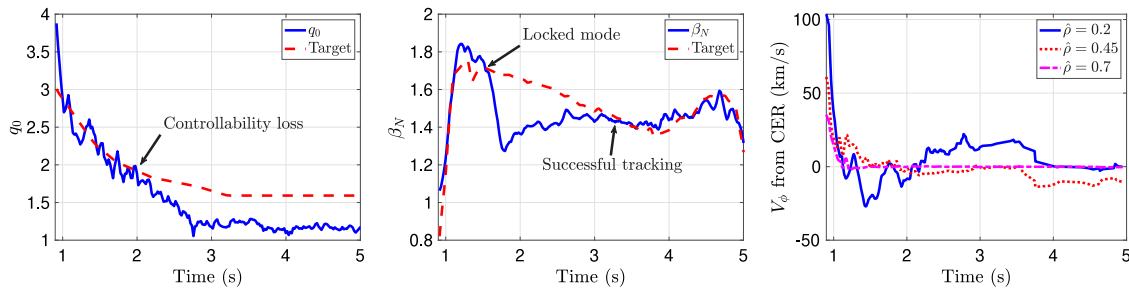


Fig. 7. Time evolutions for q_0 , β_N , and ion toroidal rotation, V_ϕ , during DIII-D shot 170685. After mode locking around $t \approx 1.5$ s, a temporary drop in β_N is found that implies a loss of controllability and makes q_0 drop. Successful β_N tracking is achieved afterwards by means of feedback. Also, V_ϕ at different spatial locations is kept near zero by the feedback-controller logic.

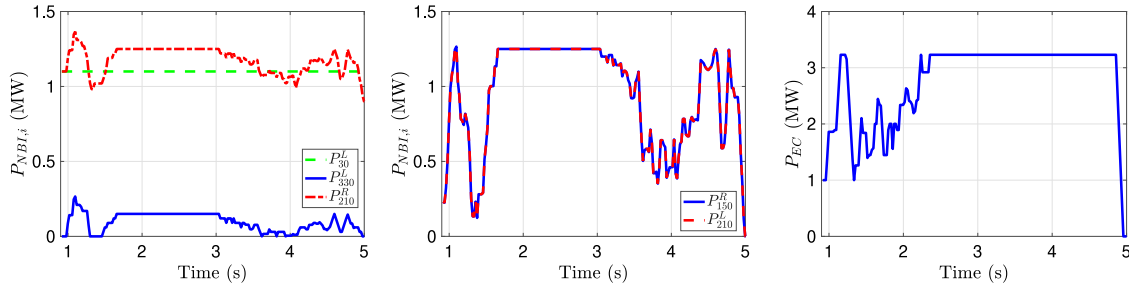


Fig. 8. Time evolutions for $P_{NBI,i}$ and P_{EC} during DIII-D shot 170685. It can be observed that the first group ($P_{30}^L + P_{330}^L \approx P_{210}^R$) and second group ($P_{150}^R = P_{210}^L$) are balanced to inject near-zero NBI torque. On the other hand, P_{EC} saturates after $t \approx 2.3$ s due to the drop in q_0 .

Fig. 5 shows the time evolution of q_0 , β_N , and ω_ϕ at $\hat{\rho} = 0.2$ during the three simulations (feedforward, target, and feedforward + feedback). When $t \leq 1.25$ s, the evolutions of q_0 , β_N , and ω_ϕ ($\hat{\rho} = 0.2$) are identical in all three simulations. After $t = 1.25$ s, the target evolutions become significantly different from the feedforward evolution due to the changes in the inputs shown in Fig. 6. By means of the feedback actions in $P_{NBI,i}$ and P_{EC} , it can be seen that the feedforward + feedback evolutions for q_0 and β_N successfully track their target evolutions with a relatively short rise time, moderate overshoot, and relatively small oscillations, and achieve a low tracking error after $t \approx 3$ s. As a result, ω_ϕ ($\hat{\rho} = 0.2$) under feedforward + feedback also tracks the target evolution, which is lower than the feedforward only evolution after $t \geq 2.5$ s.

Fig. 6 shows the time evolutions for $P_{NBI,i}$ (P_{30}^R , P_{150}^L , and P_{330}^R are not shown because they are always zero) and P_{EC} . It can be observed that there are four differences between the feedforward and target cases: (1) $P_{30}^L = P_{30}^{L,MSE} = 1$ MW in the entire target simulation, but there is a drop in P_{30}^L from 1 MW to 0 MW in the feedforward simulation at $t = 2.5$ s, (2) the counter-current NBIs (P_{210}^L and P_{210}^R) have a decrease of 0.25 MW in power during the feedforward simulation when compared to the target, (3) P_{150}^R has a drop of 0.5 MW after $t = 2.5$ s in the feedforward case compared to the target case, and (4) $P_{EC} = 0$ in the feedforward case, but $P_{EC} = 1$ MW after $t = 2.5$ s in the target case. During the feedforward + feedback simulation, the balanced-NBI configuration is used with 30L and 330L balanced by 210R in group 1, and 150R balanced by 210L in group 2. Drops in some of the feedforward + feedback powers can be seen at $t = 1.25$ s due to a decrease in the associated feedforward components, $\bar{u}^{FF,1}$. Then, the controller increases the feedback component \bar{u} , and the feedforward + feedback inputs (i.e. $\bar{u}^{FF,1} + \bar{u}$) converge toward the target inputs (i.e. $\bar{u}^{FF,2}$). Due to the relatively large differences between $\bar{u}^{FF,1}$ and $\bar{u}^{FF,2}$, convergence is achieved after short transients with moderate overshoots and oscillations. It must be emphasized that the convergence of the feedforward + feedback inputs toward the target (i.e. $\bar{u}^{FF,1} + \bar{u} \rightarrow \bar{u}^{FF,2}$) is achieved without any direct knowledge of $\bar{u}^{FF,2}$. Indirect knowledge to attain such inputs is provided to the controller through the targets q_0^{target} and β_N^{target} , as well as the dynamics

information embedded into the model-based design. On the other hand, it can be seen that P_{330}^L saturates during some small periods of time when $t \approx [1.25, 2.5]$ s, causing a small power deficit to attain a fully balanced condition in group 1.

5. Experimental testing in DIII-D

Preliminary experimental results obtained in DIII-D are shown in this section for the same plasma scenario (QH-mode) employed in the simulations from Section 4. In these experiments, 330R was unavailable, so 150R was employed instead. Also, 30L was used to obtain MSE measurements in real time with $P_{30}^{L,MSE} \approx 1.1$ MW and $P_{30}^R = 0$.

Fig. 7 shows the values for q_0 and β_N during shot 170685 as calculated by EFIT [30] as well as the ion toroidal rotation, V_ϕ , measured by charge-exchange recombination (CER) spectroscopy techniques. The feedback is active for the entire time windows shown in the figures of this section. Also, q_0^{target} is chosen so that the 3/2 surface is not present in the plasma, whereas a decrease in β_N^{target} is applied when $t \approx [1, 4]$ s. Fig. 8 shows the values of $P_{NBI,i}$ and P_{EC} during shot 170685. From Fig. 7, it can be seen that successful q_0 regulation is achieved from the beginning of the shot until $t \approx 2.2$ s and β_N regulation is achieved until $t \approx 1.5$ s, when a locked mode develops that causes a sudden drop in β_N . The gradual decrease in q_0 from $t \approx 2.2$ s till $t \approx 2.7$ s is a consequence of the drop in β_N (i.e. confinement deterioration) which reduces the electron temperature and increases the plasma resistivity, enhancing the magnetic-flux diffusion. At $t \approx 2.2$ s, it can be observed (see Fig. 8) that P_{EC} is increased and saturated ($P_{EC} \approx 3$ MW) by the feedback controller to drive q_0 to its target. Also, in order to recover β_N , the NBI powers are kept constant at the maximum attainable value ($P_{NBI} \approx 5$ MW) that maintains near-zero NBI torque (see Fig. 8). Despite saturation of the actuators, the low value of q_0 seems inevitable. On the positive side, the plasma does not disrupt, β_N is slowly increased from $t \approx 2.2$ s till $t \approx 3$ s, and β_N tracking is successfully recovered at $t \approx 3$ s (see Fig. 7), when β_N^{target} is lower. In addition, the plasma rotation measured by V_ϕ is driven to zero shortly after the beginning of the shot, and is kept low due to the near-zero NBI-torque achieved by the controller. From Fig. 8, it can be seen that the first group is balanced

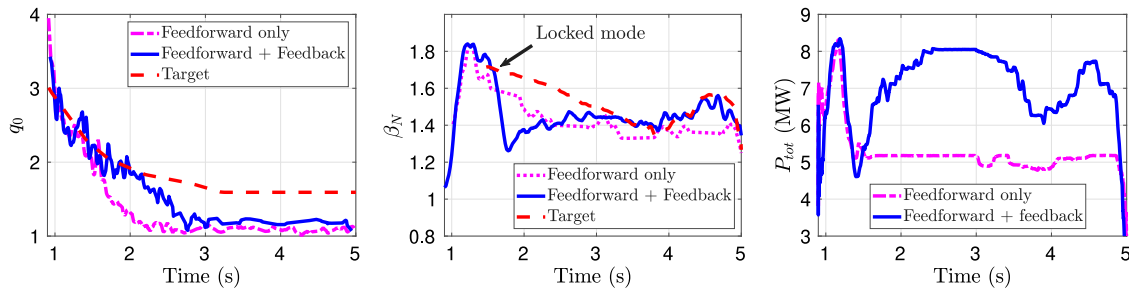


Fig. 9. Time evolutions for q_0 , β_N , and P_{tot} during DIII-D shots 170683 (feedforward only) and 170685 (feedforward + feedback), together with the targets. In general, the shot under feedback shows improved q_0 , β_N control, specially before $t \approx 2.2$ s (for q_0) and after $t \approx 3$ s (for β_N).

($P_{30}^L + P_{330}^L \approx P_{210}^R$, except at $t \approx 1.3$ s and $t \approx 4$ s due to the saturation of P_{330}^L), that the second group is also balanced ($P_{150}^R \approx P_{210}^L$), and that both groups deliver the same power. When β_N gets near its target at $t \approx 3$ s, $P_{NBI,i}$ are modulated in order to make β_N track its target until the end of the shot. On the other hand, P_{EC} is initially modulated for $q_0 + \beta_N$ control until q_0 drops and remains below its target at $t \approx 2.2$ s. After that, P_{EC} is saturated at about 3 MW to try to increase q_0 as much as possible. As introduced above, reaching q_0^{target} is not possible due to low confinement and actuator saturation.

Fig. 9 shows the values for q_0 , β_N , and $P_{tot} \triangleq P_{NBI} + P_{EC}$ in a feedforward-only shot (170683) and the same feedforward + feedback shot (170685) described in the previous paragraph. The effect of feedback control when compared with the feedforward-only shot is clear when achieving q_0 and β_N evolutions closer to their targets (which are the same targets as in Fig. 7) at the expense of using more actuation power (higher P_{tot}). In particular, q_0 regulation is specially good until $t \approx 2.2$ s under feedback. In the feedforward-only shot, q_0 drops steadily down to a value very close to 1. From $t \approx 2.2$ s till $t \approx 3$ s, q_0 is maintained more elevated under feedback, and the steady-state value of q_0 is a bit higher (≈ 1.2) when compared to the feedforward-only case ($q_0 \approx 1.1$). Regarding β_N , the main difference at around $t \approx 1.5$ s is that the value of β_N attained under feedback is slightly higher than under feedforward only. At that point, the feedforward + feedback shot experienced a locked mode, whereas the feedforward-only case did not have a locked mode. For clarity, the target β_N^{target} is not shown when $t \leq 1.5$ s (the full β_N^{target} evolution is shown in Fig. 7). After that, the lower, almost constant P_{tot} evolution in the feedforward-only case yields a lower β_N evolution which does not follow β_N^{target} , whereas successful β_N regulation is achieved after $t \approx 3$ s. Higher P_{tot} is requested during most of the feedforward + feedback shot when compared to the feedforward-only shot, specially after the appearance of the locked mode at $t \approx 1.5$ s.

6. Summary and conclusions

A control algorithm for $q_0 + \beta_N +$ NBI-torque regulation has been synthesized based on a linearized model of the current and energy dynamics. Successful control performance has been attained in 1D, fully nonlinear simulations, as well as in actual experiments in DIII-D with QH-mode plasmas. The appearance of locked modes in such QH-mode plasmas, together with the constrained NBI power for β_N control with near-zero torque and the limited EC power available, limited the controllability of q_0 . However, discharge survivability without a disruptive termination was found as the feedback controller tried to attain particular q_0 and β_N target values. In addition, low reactor-relevant rotation was attained with simultaneous $q_0 + \beta_N$ feedback regulation. This represents a first-of-its-kind control test in relatively complex control simulations, and an experimental demonstration in a present device that can preliminarily inform the design of similar control schemes in future reactor-grade tokamaks such as ITER. For instance, the EC power available in this experiment (≈ 3 MW) did not suffice to successfully regulate q_0 with balanced NBIs at near-zero

NBI torque in DIII-D. Potential developments to the scheme should consider the handling of temporary NBI saturation simultaneously with near-zero NBI torque delivery and $q_0 + \beta_N$ control.

CRediT authorship contribution statement

A. Pajares: Software, Validation, Formal analysis, Data curation, Writing, Visualization. **E. Schuster:** Conceptualization, Supervision, Project administration, Funding acquisition. **W.P. Wehner:** Software, Validation, Resources. **K.H. Burrell:** Conceptualization, Resources. **J.R. Ferron:** Resources. **M.L. Walker:** Supervision, Resources. **D.A. Humphreys:** Supervision, Project administration, Resources.

Declaration of competing interest

The authors declare that they have no known competing financial interests or personal relationships that could have appeared to influence the work reported in this paper.

Data availability

Data will be made available on request.

Acknowledgment & disclaimer

This material is based upon work supported by the U.S. Department of Energy, Office of Science, Office of Fusion Energy under Award Numbers DE-SC0010661 and DE-FC02-04ER54698.

This report was prepared as an account of work sponsored by an agency of the U.S. Government. Neither the U.S. Government nor any agency thereof, nor any of their employees, makes any warranty, express or implied, or assumes any legal liability or responsibility for the accuracy, completeness, or usefulness of any information, apparatus, product, or process disclosed, or represents that its use would not infringe privately owned rights. Reference herein to any specific commercial product, process, or service by trade name, trademark, manufacturer, or otherwise, does not necessarily constitute or imply its endorsement, recommendation, or favoring by the U.S. Government or any agency thereof. The views and opinions of authors expressed herein do not necessarily state or reflect those of the U.S. Government or any agency thereof.

Appendix A. Model of the ψ dynamics

The version of the magnetic diffusion equation [31] employed in this work is adapted from [23],

$$\frac{\partial \psi}{\partial t} = \frac{\eta}{\mu_0 \rho_b^2 \hat{F}^2} \frac{1}{\hat{\rho}} \frac{\partial}{\partial \hat{\rho}} \left(\hat{\rho} D_\psi \frac{\partial \psi}{\partial \hat{\rho}} \right) + R_0 \hat{H} \eta \left\{ \sum_{i=1}^{i=N_{NBI}} j_{NBI,i}^{dep} \frac{\sqrt{T_e}}{n_e} P_{NBI,i} + \sum_{k=1}^{k=N_{EC}} j_{EC,k}^{dep} \frac{T_e}{n_e} P_{EC,k} \right\}$$

$$\frac{R_0}{\hat{F}} \frac{1}{\partial \hat{\rho}} \left[2\mathcal{L}_{31} T_e \frac{\partial n_e}{\partial \hat{\rho}} + (2\mathcal{L}_{31} + \mathcal{L}_{32} + \alpha \mathcal{L}_{34}) n_e \frac{\partial T_e}{\partial \hat{\rho}} \right],$$

where $\eta(\hat{\rho}, t)$ is the plasma resistivity, $\hat{F}(\hat{\rho})$, $\hat{H}(\hat{\rho})$, $D_\psi(\hat{\rho})$, $L_{31}(\hat{\rho})$, $L_{32}(\hat{\rho})$, $L_{34}(\hat{\rho})$, and $\alpha(\hat{\rho})$ are geometric factors corresponding to a particular plasma equilibrium, $T_e(\hat{\rho}, t)$ and $n_e(\hat{\rho}, t)$ are the electron temperature and density, respectively, $j_{NBI,i}^{dep}(\hat{\rho})$ are model profiles that characterize the current deposition of the i th NBI, $j_{EC,k}^{dep}(\hat{\rho})$ are model profiles that characterize the deposition of the k th ECCD source, and $P_{EC,k}$ is the power of the k th ECH & CD source, where N_{EC} is the total number of ECH & CD sources. If all EC sources deliver the same amount of power, i.e. $P_{EC,k} = P_{EC}/N_{EC}$ where P_{EC} is the total EC power, then it is found that

$$\sum_{k=1}^{k=N_{EC}} j_{EC,k}^{dep} P_{EC,k} = \left[\frac{1}{N_{EC}} \sum_{k=1}^{k=N_{EC}} j_{EC,k}^{dep} \right] P_{EC} \triangleq j_{EC}^{dep} P_{EC}, \quad (A.1)$$

where $j_{EC}^{dep} \triangleq \frac{1}{N_{EC}} \sum_{k=1}^{k=N_{EC}} j_{EC,k}^{dep}$ is a single profile that characterizes the EC deposition. Additionally, the models for η , T_e and n_e are given by

$$\eta(\hat{\rho}, t) = \frac{k_{sp}(\hat{\rho}) Z_{eff}}{T_e(\hat{\rho}, t)^{3/2}}, \quad (A.2)$$

$$n_e(\hat{\rho}, t) = n_e^{prof}(\hat{\rho}) \bar{n}_e(t), \quad (A.3)$$

$$T_e(\hat{\rho}, t) = T_e^{prof}(\hat{\rho}) I_p(t) \sqrt{P_{tot}(t)}, \quad (A.4)$$

where Z_{eff} is the effective charge of the plasma ions, $k_{sp}(\hat{\rho})$, $T_e^{prof}(\hat{\rho})$, and $n_e^{prof}(\hat{\rho})$ are model profiles, $I_p(t)$ is the plasma current, $P_{tot}(t)$ is the total injected power, and $\bar{n}_e(t)$ is the line-average density. Substituting (A.2)–(A.4) into the magnetic-diffusion equation, it is found that

$$\frac{\partial \psi}{\partial t} = f_{\eta,1} \frac{\partial}{\partial \hat{\rho}} \left(f_{\eta,2} \frac{\partial \psi}{\partial \hat{\rho}} \right) u_\eta + \sum_{i=1}^{i=N_{NBI}} f_{NBI,i} \frac{P_{NBI,i}}{\sqrt{P_{tot}}} + f_{EC} \frac{P_{EC}}{P_{tot}^{1/4}} + f_{BS} \left(\frac{\partial \psi}{\partial \hat{\rho}} \right)^{-1} u_{BS}, \quad (A.5)$$

where

$$f_{\eta,1} \triangleq \frac{k_{sp} Z_{eff}}{\mu_0 \hat{\rho}^2 \hat{F}^2 (T_e^{prof})^{3/2}} \frac{1}{\hat{\rho}}, \quad (A.6)$$

$$f_{\eta,2} \triangleq \hat{\rho} D_\psi, \quad (A.7)$$

$$f_{NBI,i} \triangleq R_0 \hat{H} \frac{k_{sp} Z_{eff}}{T_e^{prof}} j_{NBI,i}^{dep} \frac{1}{I_p n_e^{prof} \bar{n}_e}, \quad (A.8)$$

$$f_{EC} \triangleq R_0 \hat{H} \frac{k_{sp} Z_{eff}}{(T_e^{prof})^{1/2}} j_{EC}^{dep} \frac{1}{\sqrt{I_p} n_e^{prof} \bar{n}_e}, \quad (A.9)$$

$$f_{BS} \triangleq R_0^2 \frac{\hat{H}}{\hat{F}} \frac{k_{sp} Z_{eff}}{(T_e^{prof})^{3/2}} \left(\frac{\partial \psi}{\partial \hat{\rho}} \right)^{-1} \left[2\mathcal{L}_{31} T_e^{prof} \frac{\partial n_e^{prof}}{\partial \hat{\rho}} + (2\mathcal{L}_{31} + \mathcal{L}_{32} + \alpha \mathcal{L}_{34}) n_e^{prof} \frac{\partial T_e^{prof}}{\partial \hat{\rho}} \right], \quad (A.10)$$

$$u_\eta \triangleq (I_p \sqrt{P_{tot}})^{-3/2}, \quad u_{BS} \triangleq \frac{\bar{n}_e}{\sqrt{I_p} P_{tot}^{1/4}}. \quad (A.11)$$

Appendix B. Discretization of the current-profile and energy dynamics using finite differences

Particularizing the magnetic-diffusion equation (6) at the interior discretization nodes $\hat{\rho}_i$, where $i = 1, 2, \dots, N$, with negligible NBI current, it is found that

$$\frac{d\psi_1}{dt} = f_{\eta,1}(\hat{\rho}_1) \frac{\partial}{\partial \hat{\rho}} \left(f_{\eta,2} \frac{\partial \psi}{\partial \hat{\rho}} \right) \Big|_{\hat{\rho}_1} u_\eta + f_{EC}(\hat{\rho}_1) \frac{P_{EC}}{P_{tot}^{1/4}} + f_{BS}(\hat{\rho}_1) \left(\frac{\partial \psi}{\partial \hat{\rho}} \right)^{-1} \Big|_{\hat{\rho}_1} u_{BS}, \quad (B.1)$$

$$\frac{d\psi_2}{dt} = f_{\eta,1}(\hat{\rho}_2) \frac{\partial}{\partial \hat{\rho}} \left(f_{\eta,2} \frac{\partial \psi}{\partial \hat{\rho}} \right) \Big|_{\hat{\rho}_2} u_\eta + f_{EC}(\hat{\rho}_2) \frac{P_{EC}}{P_{tot}^{1/4}} + f_{BS}(\hat{\rho}_2) \left(\frac{\partial \psi}{\partial \hat{\rho}} \right)^{-1} \Big|_{\hat{\rho}_2} u_{BS}, \quad (B.2)$$

⋮

$$\frac{d\psi_i}{dt} = f_{\eta,1}(\hat{\rho}_i) \frac{\partial}{\partial \hat{\rho}} \left(f_{\eta,2} \frac{\partial \psi}{\partial \hat{\rho}} \right) \Big|_{\hat{\rho}_i} u_\eta + f_{EC}(\hat{\rho}_i) \frac{P_{EC}}{P_{tot}^{1/4}} + f_{BS}(\hat{\rho}_i) \left(\frac{\partial \psi}{\partial \hat{\rho}} \right)^{-1} \Big|_{\hat{\rho}_i} u_{BS}, \quad (B.3)$$

⋮

$$\frac{d\psi_N}{dt} = f_{\eta,1}(\hat{\rho}_N) \frac{\partial}{\partial \hat{\rho}} \left(f_{\eta,2} \frac{\partial \psi}{\partial \hat{\rho}} \right) \Big|_{\hat{\rho}_N} u_\eta + f_{EC}(\hat{\rho}_N) \frac{P_{EC}}{P_{tot}^{1/4}} + f_{BS}(\hat{\rho}_N) \left(\frac{\partial \psi}{\partial \hat{\rho}} \right)^{-1} \Big|_{\hat{\rho}_N} u_{BS}. \quad (B.4)$$

For a generic function, denoted as $h(\hat{\rho}, t)$, the derivative with respect to $\hat{\rho}$ at $\hat{\rho}_i$ is approximated as

$$\frac{\partial h}{\partial \hat{\rho}} \Big|_{\hat{\rho}=\hat{\rho}_i} \approx \frac{h(\hat{\rho}_{i+1}) - h(\hat{\rho}_{i-1})}{2\Delta\hat{\rho}}, \quad (B.5)$$

so the set of N Eqs. (B.1)–(B.4) can be rewritten as

$$\frac{d\psi_1}{dt} = f_{\eta,1}(\hat{\rho}_1) \frac{f_{\eta,2}(\hat{\rho}_2) \frac{\psi_3 - \psi_1}{2\Delta\hat{\rho}} - f_{\eta,2}(0) \frac{\partial \psi}{\partial \hat{\rho}} \Big|_0}{2\Delta\hat{\rho}} u_\eta + f_{EC}(\hat{\rho}_1) \frac{P_{EC}}{P_{tot}^{1/4}} + f_{BS}(\hat{\rho}_1) \frac{2\Delta\hat{\rho}}{\psi_2 - \psi_0} u_{BS}, \quad (B.6)$$

$$\frac{d\psi_2}{dt} = f_{\eta,1}(\hat{\rho}_2) \frac{f_{\eta,2}(\hat{\rho}_3) \frac{\psi_4 - \psi_2}{2\Delta\hat{\rho}} - f_{\eta,2}(\hat{\rho}_1) \frac{\psi_2 - \psi_0}{2\Delta\hat{\rho}}}{2\Delta\hat{\rho}} u_\eta + f_{EC}(\hat{\rho}_2) \frac{P_{EC}}{P_{tot}^{1/4}} + f_{BS}(\hat{\rho}_2) \frac{2\Delta\hat{\rho}}{\psi_3 - \psi_1} u_{BS}, \quad (B.7)$$

⋮

$$\frac{d\psi_i}{dt} = f_{\eta,1}(\hat{\rho}_i) \frac{f_{\eta,2}(\hat{\rho}_{i+1}) \frac{\psi_{i+2} - \psi_i}{2\Delta\hat{\rho}} - f_{\eta,2}(\hat{\rho}_{i-1}) \frac{\psi_i - \psi_{i-2}}{2\Delta\hat{\rho}}}{2\Delta\hat{\rho}} u_\eta + f_{EC}(\hat{\rho}_i) \frac{P_{EC}}{P_{tot}^{1/4}} + f_{BS}(\hat{\rho}_i) \frac{2\Delta\hat{\rho}}{\psi_{i+1} - \psi_{i-1}} u_{BS}, \quad (B.8)$$

⋮

$$\frac{d\psi_N}{dt} = f_{\eta,1}(\hat{\rho}_N) \frac{f_{\eta,2}(1) \frac{\partial \psi}{\partial \hat{\rho}} \Big|_1 - f_{\eta,2}(\hat{\rho}_{N-1}) \frac{\psi_N - \psi_{N-2}}{2\Delta\hat{\rho}}}{2\Delta\hat{\rho}} u_\eta + f_{EC}(\hat{\rho}_N) \frac{P_{EC}}{P_{tot}^{1/4}} + f_{BS}(\hat{\rho}_N) \frac{2\Delta\hat{\rho}}{\psi_{N+1} - \psi_{N-1}} u_{BS}, \quad (B.9)$$

and the boundary conditions (7)–(8) can be rewritten as

$$\frac{\partial \psi}{\partial \hat{\rho}} \Big|_0 = \frac{-3\psi_0 + 4\psi_1 - \psi_2}{2\Delta\hat{\rho}} = 0, \quad (B.10)$$

$$\frac{\partial \psi}{\partial \hat{\rho}} \Big|_1 = \frac{3\psi_{N+1} - 4\psi_N + \psi_{N-1}}{2\Delta\hat{\rho}} = -k_I I_p. \quad (B.11)$$

Using (B.11) to substitute $\frac{\partial \psi}{\partial \hat{\rho}} \Big|_0$, $\frac{\partial \psi}{\partial \hat{\rho}} \Big|_1$, ψ_0 , and ψ_{N+1} in (B.6)–(B.9), the following compact form is found,

$$\frac{d}{dt} [\psi_1, \dots, \psi_N]^T = f_\psi(\psi_1, \dots, \psi_N, P_{NBI,1}, \dots, P_{NBI,N_{NBI}}, P_{EC}, I_p, \bar{n}_e), \quad (B.12)$$

where $f_\psi \in \mathbb{R}^N$ is a function arising from the right-hand sides in (B.6)–(B.9) with (B.11), and the dependence on I_p and \bar{n}_e arises from u_η and u_{BS} , see Eqs. (9)–(10). Adding Eq. (11) to (B.12), it is found that

$$\frac{d}{dt} [\psi_1, \dots, \psi_N, W]^T =$$

$$= f(\psi_1, \dots, \psi_N, W, P_{NBI,1}, \dots, P_{NBI,N_{NBI}}, P_{EC}, I_p, \tilde{n}_e), \quad (\text{B.13})$$

where $f \in \mathbb{R}^{N+1}$ is a function arising from the combination of f_ψ and the right-hand side of (11).

The definition of q_0 in Eq. (3) can be discretized as

$$q_0 = -\frac{B_{\phi,0}\rho_b^2}{\partial^2\psi/\partial\hat{\rho}^2|_0} = -\frac{B_{\phi,0}\rho_b^2\Delta\hat{\rho}^2}{\psi_0 - 2\psi_1 + \psi_2}, \quad (\text{B.14})$$

and using the boundary condition at $\hat{\rho} = 0$ in (B.11), it is possible to write

$$q_0 = \frac{3}{2} \frac{B_{\phi,0}\rho_b^2\Delta\hat{\rho}^2}{\psi_1 - \psi_2} \triangleq g_\psi(\psi_1, \psi_2), \quad (\text{B.15})$$

which, together with (4)–(5), can be expressed in compact form as

$$[q_0, \beta_N]^T = g(\psi_1, \psi_2, W, I_p). \quad (\text{B.16})$$

Appendix C. Analysis of the open-loop dynamics coupling via singular value decomposition

The degree of coupling between inputs and outputs in (17)–(18) can be analyzed from the singular-value decomposition of G in (25) at steady state, i.e. when $s \rightarrow 0$ [17]. Such static transfer function is denoted by G_0 , and its singular value decomposition is denoted by $G_0 = H\Sigma U^T$, where H , Σ , and U are 2×2 matrices. The diagonal matrix Σ contains the singular values σ_i ($i = 1, 2$), the principal input directions $U_i \in \mathbb{R}^2$ correspond to the columns of U , and the principal output directions $H_i \in \mathbb{R}^2$ correspond to the columns of H . Representative values of σ_i , U_i and H_i for DIII-D QH-mode plasmas are given by

$$\sigma_1 \approx 0.40, \quad U_1 \approx [0.7, 0.7]^T, \quad H_1 \approx [-0.4, 0.9], \quad (\text{C.1})$$

$$\sigma_2 \approx 0.01, \quad U_2 \approx [0.7, -0.7]^T, \quad H_2 \approx [0.9, 0.4], \quad (\text{C.2})$$

so, if $s \rightarrow 0$, it is found that $H_1\tilde{y} = \sigma_1 U_1\tilde{u}$ and $H_2\tilde{y} = \sigma_2 U_2\tilde{u}$, i.e.

$$-0.4\tilde{q}_0 + 0.9\tilde{\beta}_N = 0.4(0.7\tilde{P}_{NBI} + 0.7\tilde{P}_{EC}), \quad (\text{C.3})$$

$$0.9\tilde{q}_0 + 0.4\tilde{\beta}_N = 0.01(0.7\tilde{P}_{NBI} - 0.7\tilde{P}_{EC}). \quad (\text{C.4})$$

From (C.3)–(C.4), it can be seen that there is a tight coupling between q_0 , β_N , P_{NBI} , and P_{EC} . Therefore, a comprehensive feedback scheme for simultaneous control of $q_0 + \beta_N$ will need to synchronously use both P_{NBI} and P_{EC} . It can also be observed that U_1 is a more efficient input channel than U_2 ($\sigma_1 \gg \sigma_2$), so a feedback controller pushing along the U_1 direction (i.e. using feedback actions with the same sign and similar magnitude in \tilde{P}_{EC} and \tilde{P}_{NBI}) will generally need less power to control q_0 and β_N than along the U_2 direction (i.e. using opposite signs in \tilde{P}_{EC} and \tilde{P}_{NBI}).

References

- [1] N.A. Uckan, Confinement capability of ITER-EDA design, in: Proc. 15th IEEE/NPSS Symposium on Fusion Engineering, Vol. 1, 1993, pp. 183–186.
- [2] ITER Physics Expert Group on Confinement and Transport, et al., Chapter 2: Plasma confinement and transport, Nucl. Fusion 39 (2175) (1999).
- [3] C. Chrystal, et al., Predicting rotation for ITER via studies of intrinsic torque and momentum transport in DIII-D, Phys. Plasmas 24 (2017) 056113.
- [4] M.F. Nave, J.A. Wesson, Mode locking in tokamaks, Nucl. Fusion 30 (1990) 2575.
- [5] L. Piron, et al., 3D magnetic fields and plasma rotation in RFX-mod tokamak plasmas, Nucl. Fusion 53 (2013) 113022.
- [6] J.E. Rice, Spontaneous rotation and momentum transport in tokamak plasmas, J. Phys. Conf. Ser. 123 (2008) 012003.
- [7] J. Wesson, Tokamaks, third ed., Oxford University Press, 2004.
- [8] R. Prater, et al., Neoclassical tearing modes in DIII-D and calculations of the stabilizing effects of localized electron cyclotron current drive, in: AIP Conference Proceedings, 1999, p. 485, 261.
- [9] C.J. Rapson, et al., Experiments on actuator management and integrated control at ASDEX upgrade, Fusion Eng. Des. 123 (2017) 603–606.
- [10] M. Lehnen, et al., Disruptions in ITER and strategies for their control and mitigation, J. Nucl. Mater. 463 (2015) 39–48.
- [11] A.C. Sips, Advanced scenarios for ITER operation, Plasma Phys. Control. Fusion 47 (2005) A19.
- [12] D. Moreau, et al., Integrated magnetic and kinetic control of advanced tokamak plasmas on DIII-D based on data-driven models, Nucl. Fusion 53 (2013) 063020.
- [13] J. Barton, et al., Physics-based control-oriented modeling and robust feedback control of the plasma safety factor profile and stored energy dynamics in ITER, Plasma Phys. Control. Fusion 57 (2015) 115003.
- [14] E. Maljaars, et al., Control of the tokamak safety factor profile with time-varying constraints using MPC, Nucl. Fusion 55 (2015) 023001.
- [15] W.P. Wehner, et al., Optimal current profile control for enhanced repeatability of L-mode and H-mode discharges in DIII-D, Fusion Eng. Des. 123 (2017) 513–517.
- [16] M.D. Boyer, et al., Central safety factor and normalized beta control on NSTX-U via beam power and plasma boundary shape modification, using TRANSP for closed loop simulations, Nucl. Fusion 55 (2015) 053033.
- [17] S. Skogestad, I. Postlethwaite, Multivariable Feedback Control: Analysis and Design, Wiley-Interscience, 2005.
- [18] A. Pajares, E. Schuster, Central safety factor control in DIII-D using neutral beam injection and electron cyclotron launchers in zero input-torque scenarios, in: Proceedings of the IEEE Conference on Control Technology and Applications, 2017, p. 485, 261.
- [19] A. Pajares, E. Schuster, Current profile and normalized beta control via feedback linearization and Lyapunov techniques, Nucl. Fusion 61 (2021) 036006.
- [20] K.H. Burrell, et al., Advances in understanding quiescent H-mode plasmas in DIII-D, Phys. Plasmas 12 (2005) 056121.
- [21] IAEA Summary of the ITER Final Design Report, 2001, ITER EDA Documentation Series No. 22, IAEA, Vienna.
- [22] TRANSP Official website, URL <https://transp.pppl.gov/index.html>.
- [23] J. Barton, et al., Physics-based control-oriented modeling of the safety factor profile dynamics in high performance tokamak plasmas, in: Proc. IEEE Conference on Decision and Control, CDC, 2013, pp. 4182–4187.
- [24] M. Erba, et al., Validation of a new mixed Bohm/Gyro-Bohm model for electron and ion heat transport against the ITER, Nucl. Fusion 38 (1998) 1013.
- [25] W.M. Tang, et al., Microinstability-based model for anomalous thermal confinement in tokamaks, Nucl. Fusion 26 (1986) 1605.
- [26] T. Onjun, et al., Models for the pedestal temperature at the edge of H-mode tokamak plasmas, Phys. Plasmas 9 (2002) 5018.
- [27] A. Pajares, E. Schuster, Integrated robust control of the global toroidal rotation and total plasma energy in tokamaks, IEEE Trans. Plasma Sci. 48 (6) (2020) 1606–1612.
- [28] J.E. Kinsey, et al., The first transport code simulations using the trapped Gyro-Landau-fluid model, Phys. Plasmas 15 (055908) (2008).
- [29] A. Pankin, et al., The tokamak Monte Carlo fast ion module NUBEAM in the National Transport Code Collaboration library, Comput. Phys. Comm. 159 (2004) 157–184.
- [30] J.R. Ferron, et al., Real time equilibrium reconstruction for tokamak discharge control, Nucl. Fusion 38 (1998) 1055.
- [31] F. Hinton, R. Hazeltine, Theory of plasma transport in toroidal confinement systems, Rev. Modern Phys. 48 (1976) 239–308.